Durability of Silicon Pin-Joints for Microrobotics

Daniel S. Contreras, Kristofer S. J. Pister
Electrical Engineering and
Computer Sciences
University of California, Berkeley
Berkeley, California 94707-1774
Email: dscontreras@berkeley.edu

***Abstract*—This work presents the initial characterization of planar silicon pin-joints for use in linkages for walking microrobot legs. A major goal in walking microrobotics is the creation of robust leg structures driven by low-power motors capable of lifting a 20mg mass and propelling it forward. Hinged joint structures, rather than stiff flexures, are ideal for this task. However, since joints are not fully rigid structures, the possibility of pull-out failure is important to take into account. The joints we use are fabricated in a silicon-on-insulator (SOI) process. They have demonstrated pull-out forces ranging from 1mN to 29mN, well over the strength of our motor designs and capable of handling the intended mass of the robot. Additionally, the frictional coefficient during pull-out was found to be dependent on the load from the joint holder.**

***Index Terms*—MEMS, silicon, microrobot, joints, legs, friction.**

I. Introduction

The field of microelectromechanical systems (MEMS) based microrobotics has seen significant strides in the last few decades. Jumping microrobots incorporating microscale elastomers with MEMS structures have shown promise, launching themselves over 32cm into the air, over 80x their own height [1]. There has also been progress in the field of flying microrobots using piezoelectric actuators to flap a set of insect-like wings [2]. In terms of ground-based microrobotics, walking microrobots have used a variety of methods for locomotion such as thermal actuators and capacitive-coupling to a substrate to move electrostatically [3], [4].

The robots described above all rely on some method of beam flexure in order to move. Some of these stiff flexures rely on high force density motors to bend, such as thermal actuators and piezoelectric actuators. If system autonomy is a main concern in the final robot design, these actuators are not ideal since they usually draw a large amount of power (over 100mW).

Electrostatic inchworm motors [5] consume much less power and can be driven by energy scavenging technologies such as solar cells. The main disadvantage of electrostatic motors is that they typically have less force density than their thermal and piezoelectric counterparts [6]. In order to effectively use electrostatics to drive a microrobot linkage, the linkage must be flexible enough to move without resistance but still stiff enough to support the mass of the robot.

Hinged linkage structures work well for this purpose. Hinges are easy to bend with low force actuators. Additionally, they do not store a large amount of unrecoverable energy in their bending, as with stiffer flexures. A previous generation of solar-powered walking silicon microrobots used hinged linkages to actuate a set of legs [7]. This robot had a number of issues in terms of fabrication and process design. The device had low yield, since it was fabricated in a two-layer polysilicon on silicon-on-insulator (SOI) process. Additionally, the robot was limited to thin-films to form the hinges. This fragile material limits the maximum forces the joints can handle.

Previous work looked into using pivot-based linkages fabricated in the plane of the wafer [8]. A combination of this planar design with 3D microassembly is one potential avenue for overcoming this planar limitation [9]. A complex leg with 2 degrees-of-freedom (DOF) can be fabricated and driven by electrostatic actuators in the plane of the wafer, then assembled in a later step such that the leg can actuate on the ground. The 2-DOF leg would allow the robot to fully lift it's body in the vertical direction and move in the horizontal direction. Fig. 1 shows a preliminary design of the 2-DOF leg of such a microrobot.

This work presents the initial investigation of planar silicon pin-joints that will be the basic building block for microrobotic linkages. The main focus is on the pull-out force of the joint, which determines if the joint will be safe under the load of the driving motor and robot body without popping out the joint holder in-plane. Fig. 1 shows a joint with this specific load condition in the leg linkage. For some of the microrobots described previously, tension is not an issue since their flexures are fully rigid [1]–[4]. Our joints have the advantage of rotating under little force, but could potentially suffer due to the hinge being a failing point under tension.

II. Theory

A. Basic Joint Design

The basic unit of these linkages is a simple joint structure, shown in Fig. 2. The silicon pin-joints described in this work are formed by a C-shaped holder surrounding a concentric circle, serving as the rotating element. The rotating element and joint holder are connected by a weak rotary spring, holding the pieces together during processing and allowing the joint to rotate without much torsional resistance. The gap inside the joint is determined by the minimum feature size of the process (2μm). This minimizes any non-rotational movement within the joint.

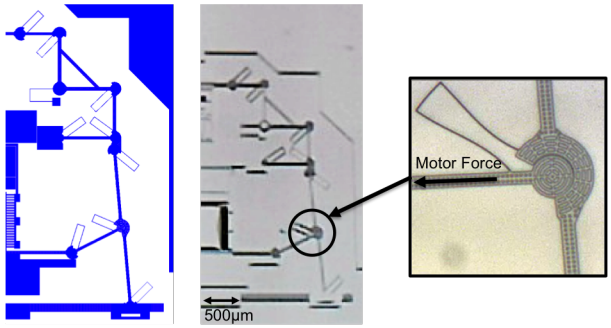

Fig. 1. *Left* : A preliminary robot leg design in layout *Center* : The robot leg fabricated. *Right* : The detail shows a joint under the tension loading case described in this paper.

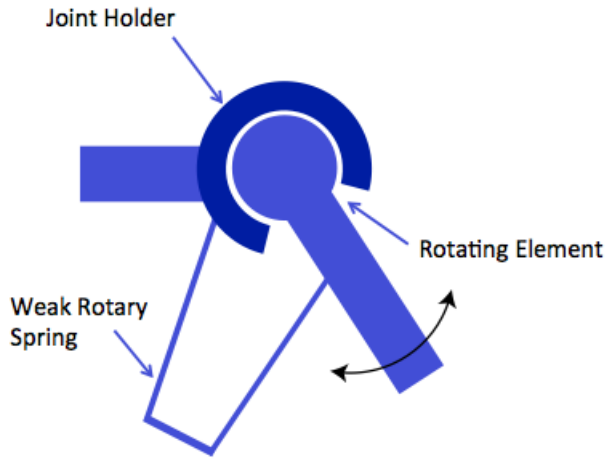

Fig. 2. A diagram of the basic joint design.

B. Joint Constraints

The ideal joint would have rotational motion as close to 180° as possible, be able to withstand large forces under tension and compression, and rotate without friction under large loads. For our joints, there is a design trade-off between having large rotational motion and withstanding forces while under tension. Since our joints are not stiff flexures as in the microrobot designs already discussed in [1]–[4], there is the possibility that the joint can slip out of its socket. A large joint opening would allow for greater travel but would also let the joint slip out more easily.

C. Pull-Out Force

The theory we used on the bending of thick curved beams was adapted from [10]. The force resisting pull-out is a function of the bending of the C-shaped holder. The bending of the joint holder will put a force on the rotating element. The rotating element must then overcome the frictional force from this load to break the joint.

1) Curved Beam Bending: To determine the bending of the joint holder, we need to use Castigliano's theorem. Fig. 3 shows the joint before and during pulling and the free-body

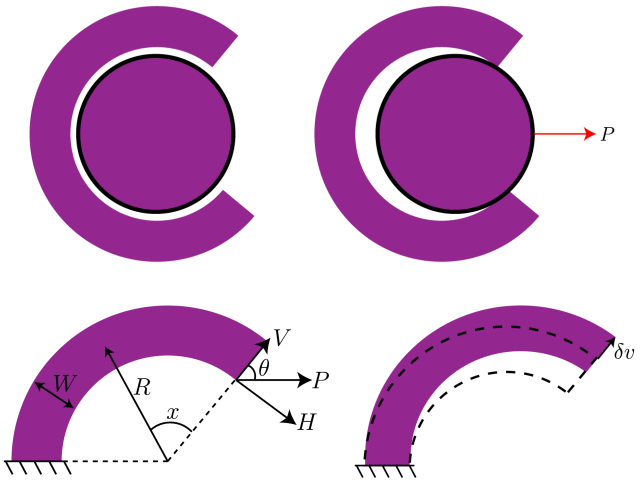

Fig. 3. *Top* : The motion of the joint as it is pulling out of the joint holder. *Bottom* : The corresponding free-body diagram of the joint holder showing the loading on the joint holder from the rotating element being pulled out (left). The radial deflection of the joint holder, δv, in the direction of V as the rotating element is pulled out (right). We take advantage of the symmetry of the joint about the horizontal axis to analyze a simpler half model.

TABLE I
MAXIMUM RADIAL DISPLACEMENT OF JOINT HOLDERS FOR CORRESPONDING ANGULAR OPENINGS

Angle of Opening (degrees)	110	115	120	125	130	135	140
Radial Deflection (μm)	9.7	8.0	6.4	5.0	3.7	2.5	1.5

diagram of the joint holder. With a load P along the horizontal axis we can decompose this force into components in the polar axes centered on the joint, indicated by H and V. These components are $H = P\sin\theta$ and $V = P\cos\theta$, where θ is the angle of the joint opening from the horizontal.

Since H is offset from the neutral axis of the beam, it will contribute to a moment at the tip. Assuming this is a pure moment, it will be given as $M_o = H\frac{W}{2}$, where W is the width of the curved cross-section. The overall moment, shear force, and axial force are given by

$$M_x = VR\sin x + M_o \tag{1}$$

$$V_x = V\cos x \tag{2}$$

$$N_x = V\sin x \tag{3}$$

where R is taken as the line from the center of the joint to the neutral axis of the joint holder, which is displaced from the centroidal axis of the holder due to the curvature.

The complementary energy of the beam will be given by

$$U = \int \frac{M_x^2}{2AEe}dx + \int \frac{FV_x^2R}{2AG}dx + \int \frac{N_x^2}{2AE}dx - \int \frac{M_xN_x}{AE}dx \tag{4}$$

where A is the cross-sectional area of the beam, E is the Young's Modulus of the material, e is the offset of the neutral axis from the centroidal axis (the moment is taken about the neutral axis), F is the shape factor of the cross-section, and G is the shear modulus. The integrals are taken over the angular length of the joint holder. This parameter is varied over the test structure array.

According to Castigliano's theorem, the deflection along the axis of interest will be given by the partial derivative of the complementary energy with respect to the load in the axis of interest. In this case, the deflection in the radial direction (along the load V) caused by the rotating element sliding into and along the joint holder, is given by

$$\delta v = \frac{\partial U}{\partial V} \tag{5}$$

By using equation 4 in equation 5 we can find the deflection as a function of the radial reaction force from the beam, F_v, with the radial stiffness, k_{rad}, as a constant of proportionality

$$F_v = 2k_{rad}\delta v \tag{6}$$

where, since our analysis looks at a half model, the final stiffness is doubled. The displacement we care about for the joint holder is the point at which the rotating element fits between the opening in the holder, assuming this happens before the joint holder fractures from stress. We can find the displacement necessary to fit the maximum width of the rotating element through the joint holder opening from the drawn geometry. This displacement is shown in Fig. 3. Each angular opening will have a corresponding maximum deflection, given in Table I.

We can break down the reaction force F_v into horizontal and vertical components. The horizontal component will not have a surface to act on at the moment of pull-out so it will have a negligible effect. The vertical component will act as a normal force, F_n, on the joint holder, which will create the frictional force directly opposing the pull-out force, proportional to the frictional coefficient μ_f. This will be given by

$$P = \mu_f F_v \sin\theta = \mu_f F_n \tag{7}$$

Values for silicon-on-silicon frictional coefficients at the microscale vary widely and are highly dependent on the contact areas and surface forces between the faces [11]–[13].

For our initial designs we relied on a frictional coefficient of 0.38 to approximate the regime of the expected forces [13]. For the purpose of our approximation we chose spring constants for the angular openings that best fit the experimental data we found. The pull-out forces calculated from the theory using this spring constant range from 1mN to over 50mN, depending on the geometry. The force gauges used to measure these values must be able to measure and withstand these loads.

D. Pull-Out Force Gauge

To measure the pull-out force we relied on simple spring-based Vernier gauges attached to the structures. The basic

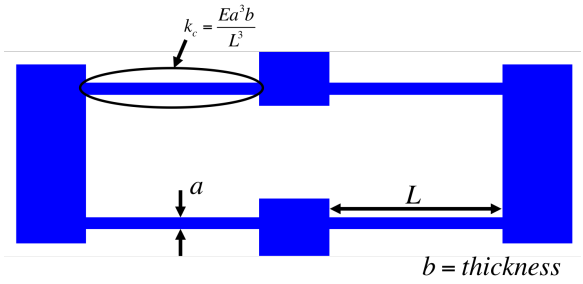

Fig. 4. Detail of the force gauge used to measure the pull-out force with dimensions labeled. The spring constant of a single beam is given by k_c.

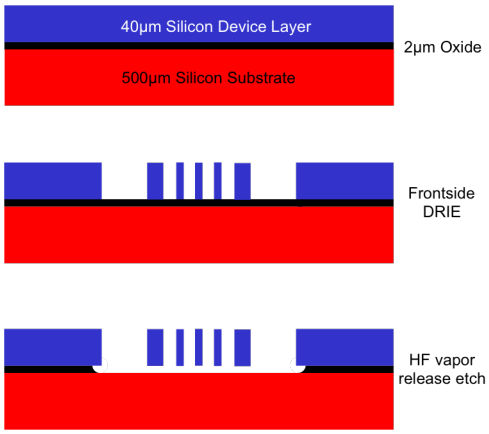

Fig. 5. A cross-section of the simple SOI process used to fabricate the joints.

gauge design is shown in Fig. 4. The spring constant of the gauge can be found by finding the combination of the spring constants of the four fixed-guided beams that make up the structure. This combination will be that of two parallel fixed-guided beams in series with another pair of fixed-guided beams in parallel. The total stiffness of the gauge is given by

$$k_{gauge} = \frac{Ea^3b}{L^3} \tag{8}$$

where E is the Young's Modulus of the material, a is the width in the direction of bending, b is the thickness of the beam, and L is the length of the beam. The gauges were designed to deflect up to 5µm in the regime of the expected forces, 1mN to 100mN. In our measurements we tracked the verniers with 0.1µm accuracy. The measurement resolution is given by the optical camera system used to measure the displacement of the gauge. Table II gives the beam widths, expected analytical spring constants, and the measured spring constants for each gauge used.

III. Fabrication

These structures were fabricated in a silicon-on-insulator (SOI) process. A process cross-section is shown in Fig. 5. SOI wafers were purchased with a thick substrate of silicon (500µm), a thin oxide layer (2µm), and 40µm of device layer silicon. The device layer silicon is used for all structures. This layer is etched using deep reactive ion etching (DRIE),

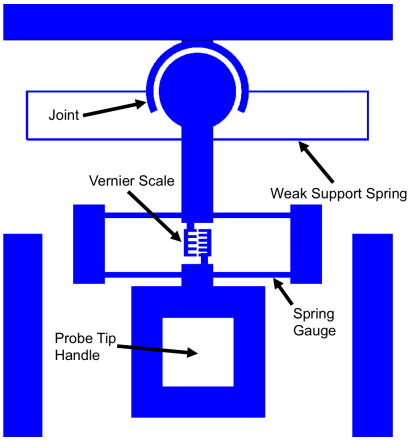

Fig. 6. Layout of a pull-out force test structure with pieces labeled. The test structure is composed of a joint, weak springs to tether the joint to the substrate, a spring-based gauge with a vernier scale to read displacements, and a handle to manipulate with a probe-tip.

a process that produces structures with relatively straight sidewalls. This produces a 40μm layer of silicon in the shape of the pattern from Fig. 6. The structure is then released by a timed etch of the middle oxide layer in a vapor-phase hydrofluoric acid (HF) etch. The structure is designed such that the HF etch will undercut some structures and leave other structures anchored to the substrate. Large structures such as the trusses on the sides of the spring gauge and the joint itself can be released by using etch-holes.

IV. Method

The test structures were varied in terms of the angular size of the opening in the joint holder and the radial width of the joint holder.

Fig. 7 shows a pull-out test being performed. A tungsten probe tip on a micromanipulator stage was used to pull the structures apart. The pull-out test structure was designed with handles to fit a probe-tip, shown in Fig. 6. The pull-out process was captured on video for analysis. Using video tracking software, we were able to calculate the displacement of the Vernier gauge. This displacement would then be translated to a force according to the specific gauge's spring constant. The tracking software used to track the displacement performs a bicubic interpolation on the search area when tracking a feature in a series of images in order to achieve sub-pixel precision. Images were tracked with 0.25 pixel accuracy, corresponding to 0.1μm resolution. This value was taken as the dominating source of error.

V. Results

Fig. 8 shows plots of the measured pull-out force vs. the calculated applied normal load for each angular joint opening. The slopes of these lines are taken as the frictional coefficient for that specific joint holder opening. Fig 9 shows experimental results plotted alongside theoretical values, with frictional coefficients for the theoretical lines taken from Fig 8. Table II gives the measured spring constants for the gauges.

TABLE II
Analytical, Measured, and Simulated Spring Constants for the Pull-out Force Gauges with Respect to Beam Width

Drawn Beam Width (μm)	Analytical Spring Constant (N/m)	Simulated Spring Constant (N/m)	Measured Spring Constant (N/m)
6.5	1900	1900	1100
10.5	7800	6600	4600
15.5	25200	16100	13300

A. Force Gauge Calibration

The spring-based force gauges attached to the pull-out structures were calibrated using a Dage Series 4000 wire bond shear force tester. The force tester displaces the spring gauge until it breaks and then generates a force vs. displacement curve. The slope of the linear portion of the force vs. displacement curve is taken as the measured spring constant. The value of the predicted spring constants and the spring constants measured using the force tester are shown in Table II. Additionally, the gauges were simulated using CoventorWare MEMS Design Software. The values are given with respect to the drawn beam widths.

The measured value for the stiffest gauge is off from the analytical result by a factor of 1.9 for the stiffest gauge. The measured value matches more closely to the simulation, but is still off by over 20%. An explanation for this could be a combination of parasitic processing effects from the DRIE and errors in the boundary conditions of the spring gauge analysis.

Unintended lateral etching from the DRIE could make the beams smaller than the drawn beam widths, greatly affecting the beam stiffness. Additionally, a phenomenon in DRIE of SOI wafers known as footing, in which the bottoms of structures are unintentionally damaged by deflected ions due to charge build-up on the oxide layer, could also contribute to lowering of the spring constant. A uniform lateral etch of 0.5μm, which we have observed in our processing, would explain the discrepancy for the 6.5μm beam gauge.

For the stiffer gauges, we look at the boundary conditions of the beams. Simulations indicate bending in the trusses of the gauge, meaning there is some rotation at the boundary which was assumed to be fixed in the derivation of equation 8. Since there is rotation, the boundary of the truss-ends of the beams is not perfectly rigid, leading to a softening of the spring constant. This in combination with lateral etching could explain the measured spring constant being so low for the stiffer gauges.

B. Stiffness Calculations and Friction

Fig. 8 plots the pull-out force against the calculated normal load, which according to equation 7 are proportional by μ_f. The linear relationship is consistent with our theory. Fig. 9 shows the experimental data with a theoretical fit where the frictional coefficient is taken from the slopes of the linear fits in Fig. 8. Initially, the theoretical prediction assumed a load-independent friction coefficient of 0.38, a value within the range of previous experiments with silicon-on-silicon DRIE sidewall friction [13]. This value greatly overestimated the

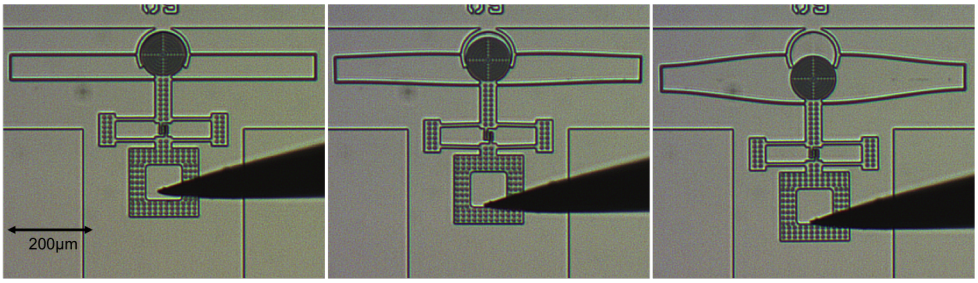

Fig. 7. A joint test structure before (left), during (center), and after (right) a pull-out test is performed. The tungsten probe tip is shown in the handle of the structure.

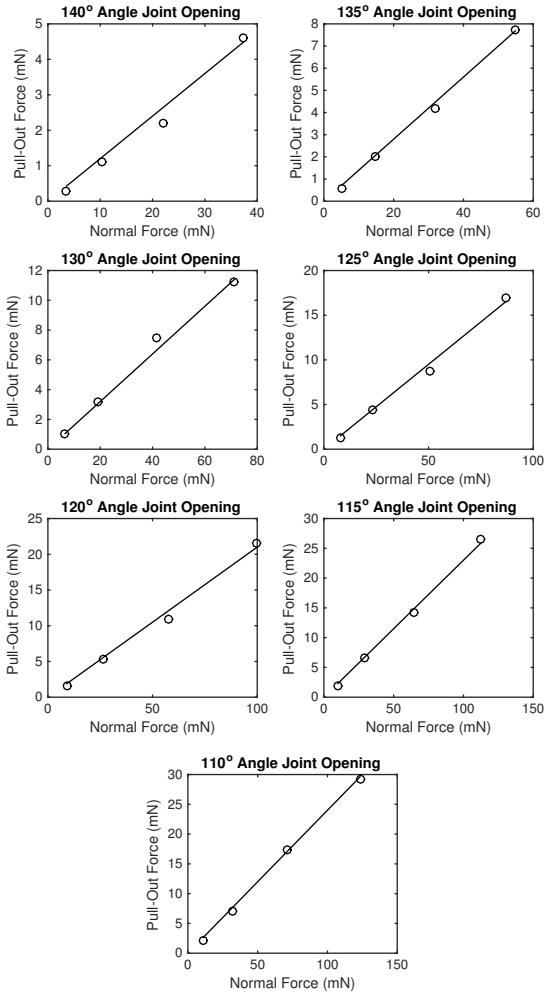

Fig. 8. The measured pull-out force vs. the normal force applied to the joint from the joint holder for each of the angular openings. The slope of the linear fit is taken as the frictional coefficient for that specific angular opening.

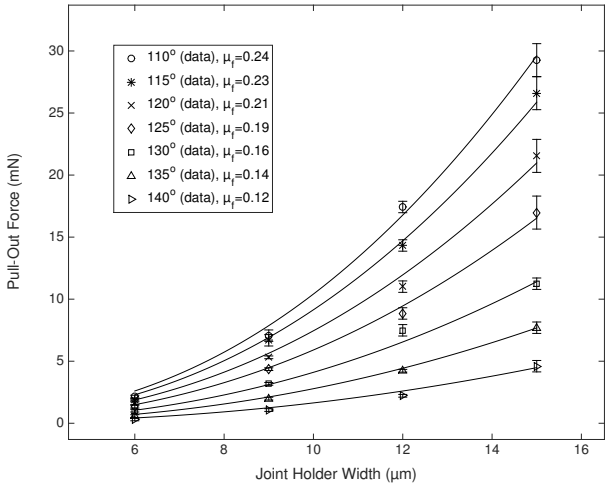

Fig. 9. Plot of the theoretical values of the pull-out force and the experimental data found from our test structures. The legend labels the data points with the corresponding angular opening. Solid lines, from top to bottom, are the theoretical fits for 110°, 115°, 120°, 125°, 130°, 135°, 140° openings in the joint holders. Frictional coefficients for the theoretical lines were taken from the linear fits in Fig. 8. These frictional coefficient values are given in the legend with respect to their angular opening size data.

experimental results, sometimes by as much as a factor of 2. It was also apparent that the friction force was dependent on the normal force.

The results in [13] calculated the frictional coefficients between large areas of single crystal silicon. For smaller contact areas and weaker loads, as with our joints, surface interactions between the silicon sidewalls could be weaker, making frictional forces lesser and lowering the coefficient. Furthermore, the DRIE process used to create these structures has a number of parasitic effects that could lead to reduction of the predicted frictional coefficients. DRIE creates scalloped sidewalls, which could also impact the friction coefficient by reducing the contact area between the sliding surfaces. Also, as stated in section V-A, footing damage is another issue inherent to DRIE that could further reduce the contact area.

In addition to changes in the expected frictional coefficient, change in the expected stiffness of the joint holder due to processing is another factor that could reduce the expected pull-out force, similar to the case with the force gauges described above. Accounting for a typical 0.5μm lateral etch in our theory by narrowing the beam widths and accounting for smaller displacements, the spring constants for the stiffest joints are reduced by as much as 10%. This is even more apparent in the weakest joints, where the stiffnesses are 30% weaker.

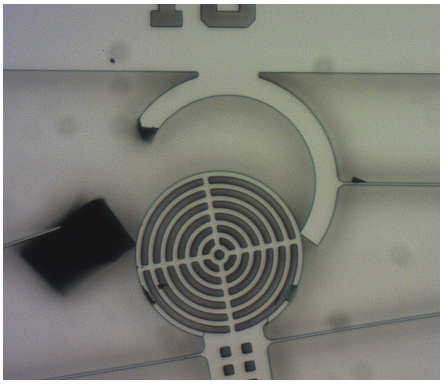

Fig. 10. The fractured joint of a test structure with a joint holder width of 15μm and an angular opening of 110°.

C. Fracture

In some cases, mainly with the thickest joint holders (15μm) with the smallest angular opening (110°), the joint holder would fracture before the rotating element came out. This fracture usually occurred along the length of the joint holder arm. This is shown in Fig. 10. In these cases, fracture was the limiting case of joint durability and not the pull-out force as we have defined.

Fracture along the arm is in agreement with the moment definition in equation 1. The stress in the beam is proportional to the moment, which is proportional to the sine of the angular position along the beam length, measured from the opening. Thus the maximum of the moment will occur at 90° which is approximately where it occurs in Fig. 10.

D. Influence on Motor Design

The forces required to break the joint while in tension are shown to be far above the intended designed motor force output. Inchworm motors are a type of linear electrostatic actuator with force densities as high as 2mN/mm^2 [5], [14].

E. Other Aspects of Joint Life

The pull-out force gives an upper limit for the in-plane forces that our robot can withstand, in tension. By simply reversing the direction we push the gauges, we can see when the joints break under compression. Preliminary results show that the joints can survive compressive loads beyond the stress failure limits of the stiffest gauge, corresponding to approximately 100mN.

The lower limit for in-plane forces, the minimum force that has to be applied to these joints to move at all, will be a function of the friction within a joint under a certain load as the joint is rotating. Ongoing work will address this other critical factor of the joints.

VI. Conclusion

This work investigated the durability of silicon pin-joints for use in walking microrobot legs. Test structures were designed to measure the force at which the joints failed under tension. The pin-joint test structures are fabricated in a silicon-on-insulator process. The test structures demonstrated pull-out failure forces ranging from 1mN to 29mN, depending on the geometry of the joints. The value of the frictional coefficient was found to vary with the size of the applied load. These forces are far above the regime of the forces exerted by the intended motor designs.

Acknowledgment

Special thanks to the staff of the UC Berkeley Marvell Nanofabrication Laboratory for their continued support in this project.

References

[1] A. P. Gerratt and S. Bergbreiter, "Incorporating compliant elastomers for jumping locomotion in microrobots," *Smart Materials and Structures*, vol. 22, no. 1, p. 014010, Jan. 2013.

[2] Z. E. Teoh, S. B. Fuller, P. Chirarattananon, N. O. Prez-Arancibia, J. D. Greenberg, and R. J. Wood, "A hovering flapping-wing microrobot with altitude control and passive upright stability," in *Intelligent Robots and Systems (IROS), 2012 IEEE/RSJ International Conference on*. IEEE, 2012, pp. 3209–3216.

[3] T. Ebefors, J. U. Mattsson, E. Klvesten, and G. Stemme, "A walking silicon micro-robot," in *Proc. Transducers 99*. Citeseer, 1999, pp. 1202–1205.

[4] B. R. Donald, C. G. Levey, C. D. McGray, I. Paprotny, and D. Rus, "An untethered, electrostatic, globally controllable MEMS micro-robot," *Microelectromechanical Systems, Journal of*, vol. 15, no. 1, pp. 1–15, 2006.

[5] R. Yeh, S. Hollar, and K. Pister, "Single mask, large force, and large displacement electrostatic linear inchworm motors," *Journal of Microelectromechanical Systems*, vol. 11, no. 4, pp. 330–336, Aug. 2002.

[6] D. J. Bell, T. J. Lu, N. A. Fleck, and S. M. Spearing, "MEMS actuators and sensors: observations on their performance and selection for purpose," *Journal of Micromechanics and Microengineering*, vol. 15, no. 7, pp. S153–S164, Jul. 2005.

[7] S. Hollar, A. Flynn, C. Bellew, and K. S. J. Pister, "Solar powered 10 mg silicon robot," in *Micro Electro Mechanical Systems, 2003. MEMS-03 Kyoto. IEEE The Sixteenth Annual International Conference on*. IEEE, 2003, pp. 706–711.

[8] A. Mehta and K. Pister, "Flexure-Based Two Degree-of-freedom Legs for Walking Microrobots," in *Proceedings of IMECE, 2006*. ASME, Nov. 2006.

[9] M. E. Last, V. Subramaniam, and K. S. Pister, "A Microassembled Large-Deflection Tip/Tilt Micromirror from a Single-Mask DRIE Process," in *Solid-State Sensors, Actuators and Microsystems Workshop, Hilton Head Island, South Carolina*, 2006.

[10] W. Young, R. Roark, and R. Budynas, *Roark's formulas for stress and strain*. McGraw-Hill, 2002.

[11] Q. Chen and G. P. Carman, "Microscale tribology (friction) measurement and influence of crystal orientation and fabrication process," in *Micro Electro Mechanical Systems, 2000. MEMS 2000. The Thirteenth Annual International Conference on*. IEEE, 2000, pp. 657–661.

[12] W. Wang and et. al, "Friction and wear properties in MEMS," *Sensors and Actuators A: Physical*, vol. 97-98, pp. 486–491, Apr. 2002.

[13] U. Beerschwinger, R. Reuben, and S. Yang, "Frictional study of micro-motor bearings," *Sensors and Actuators A: Physical*, vol. 63, no. 3, pp. 229 – 241, 1997.

[14] I. Penskiy and S. Bergbreiter, "Optimized electrostatic inchworm motors using a flexible driving arm," *Journal of Micromechanics and Microengineering*, vol. 23, no. 1, p. 015018, Jan. 2013.